

# The tidal parameters of TRAPPIST-1 b and c

R. Brasser<sup>1</sup>, A. C. Barr<sup>2</sup> and V. Dobos<sup>3,4,5</sup>

<sup>1</sup> Earth Life Science Institute, Tokyo Institute of Technology, Meguro, Tokyo 152-8551, Japan

<sup>2</sup> Planetary Science Institute, 1700 East Fort Lowell, Suite 106, Tucson, AZ, 85719, USA

<sup>3</sup> Konkoly Observatory, Research Centre for Astronomy and Earth Sciences, Hungarian Academy of Sciences, H-1121 Konkoly Thege Miklós út 15-17, Budapest, Hungary

<sup>4</sup> Geodetic and Geophysical Institute, Research Centre for Astronomy and Earth Sciences, Hungarian Academy of Sciences, H-9400 Csatai Endre u. 6-8, Sopron, Hungary

<sup>5</sup> MTA-ELTE Exoplanet Research Group, 9700, Szent Imre h. u. 112, Szombathely, Hungary

3 May 2019

## ABSTRACT

The TRAPPIST-1 planetary system consists of seven planets within 0.05 au of each other, five of which are in a multi-resonant chain. These resonances suggest the system formed via planet migration; subsequent tidal evolution has damped away most of the initial eccentricities. We used dynamical N-body simulations to estimate how long it takes for the multi-resonant configuration that arises during planet formation to break. From there we use secular theory to pose limits on the tidal parameters of planets b and c. We calibrate our results against multi-layered interior models constructed to fit the masses and radii of the planets, from which the tidal parameters are computed independently. The dynamical simulations show that the planets typically go unstable 30 Myr after their formation. Assuming synchronous rotation throughout we compute  $\frac{k_2}{Q} \gtrsim 2 \times 10^{-4}$  for planet b and  $\frac{k_2}{Q} \gtrsim 10^{-3}$  for planet c. Interior models yield  $(0.075 - 0.37) \times 10^{-4}$  for TRAPPIST-1 b and  $(0.4 - 2) \times 10^{-4}$  for TRAPPIST-1 c. The agreement between the dynamical and interior models is not too strong, but is still useful to constrain the dynamical history of the system. We suggest that this two-pronged approach could be of further use in other multi-resonant systems if the planet’s orbital and interior parameters are sufficiently well known.

**Key words:** celestial mechanics - planets and satellites: dynamical evolution and stability - planets and satellites: formation

## 1 INTRODUCTION

The star TRAPPIST-1 is an ultracool M-dwarf that harbours seven roughly Earth-sized planets (Gillon et al. 2017). All of the planets orbit within 0.07 au of the star, and have orbital periods from 1.5 to 19 days (Gillon et al. 2017; Wang et al. 2017; Grimm et al. 2018). Their orbits are slightly eccentric, and the outer five planets are in a multi-resonant chain which probably maintains the orbital eccentricities over time (Unterborn et al. 2018; Luger et al. 2017; Grimm et al. 2018). All of the planets have a density intermediate between the densities of compressed water ice and the Earth’s inner core (Gillon et al. 2017; Wang et al. 2017; Unterborn et al. 2018; Grimm et al. 2018; Barr et al. 2018), implying solid planets composed of rock, metal, and ice (see Figure 1). Despite their proximity to the TRAPPIST-1 star, the current stellar flux on each planet is modest, suggesting effective black-body surface temperatures ranging from 400 K to 167 K (Wang et al. 2017). Basic orbital and physical quantities for these planets are listed in Table 1.

The planets’ eccentric orbits and short orbital periods raise the possibility that tidal dissipation may be a significant heat source in their interiors (Luger et al. 2017; Barr et al. 2018), both now and in the past. Barr et al. (2018) showed that the planets’ proximity to the central star and their eccentric orbits leads to interior geo-

dynamics similar to that expected in the tidally heated satellites of the outer planets, specifically the inner Galilean satellites of Jupiter (Khurana et al. 2011). Several of the TRAPPIST-1 planets could have partially molten rock mantles arising from a balance between heat generation by tides and heat transport by solid-state convection. These conclusions remain valid despite recent updates to the masses and radii of the TRAPPIST-1 planets (Dobos et al. 2019).

Although the TRAPPIST-1 star is thought to be approximately 8 Gyr old, albeit with a large uncertainty (Burgasser & Mamajek 2017), initial N-body simulations of the system’s evolution have shown that the planets’ orbits may only be stable in their present configuration for  $\sim 0.5$  Myr (Gillon et al. 2017). Torques between the planets and the TRAPPIST-1 star can cause changes in the semi-major axes of the planets, and eccentricity damping by tidal dissipation can cause the orbits to circularize. Eccentricity damping is known to enhance the system’s stability, with the damping rate controlled by the planets’ internal rigidity and viscosity through the value of the  $k_2$  Love number, which describes how the planet’s gravitational potential changes in response to tidal deformation, and the tidal quality factor,  $Q$ , which is a measure of how many orbital periods are needed to damp the tidal energy (Murray & Dermott 1999a). The tidal torque additionally depends on the principal moment of inertia coefficient,  $C = I/M_{\text{pl}}R_{\text{pl}}^2$ , where  $I$  is the mo-

**Table 1.** Semi-major axes ( $a$ ), eccentricities ( $e$ ), masses ( $M_{\text{pl}}$ , scaled by Earth’s mass,  $M_{\oplus} = 5.98 \times 10^{24}$  kg), and radii ( $R_{\text{pl}}$ , scaled by Earth’s radius,  $R_{\oplus} = 6371.8$  km) for the seven TRAPPIST-1 planets from [Grimm et al. \(2018\)](#) and [Delrez et al. \(2018\)](#).

| Planet | $a$ (AU)   | $e$     | $M_{\text{pl}} (M_{\oplus})$ | $R_{\text{pl}} (R_{\oplus})$ |
|--------|------------|---------|------------------------------|------------------------------|
| b      | 0.01154775 | 0.00622 | $1.017^{+0.154}_{-0.143}$    | $1.121^{+0.031}_{-0.032}$    |
| c      | 0.01581512 | 0.00654 | $1.156^{+0.142}_{-0.131}$    | $1.095^{+0.030}_{-0.031}$    |
| d      | 0.02228038 | 0.00837 | $0.297^{+0.039}_{-0.035}$    | $0.784^{+0.023}_{-0.023}$    |
| e      | 0.02928285 | 0.00510 | $0.772^{+0.079}_{-0.075}$    | $0.910^{+0.026}_{-0.027}$    |
| f      | 0.03853361 | 0.01007 | $0.934^{+0.080}_{-0.078}$    | $1.046^{+0.029}_{-0.030}$    |
| g      | 0.04687692 | 0.00208 | $1.148^{+0.098}_{-0.095}$    | $1.148^{+0.032}_{-0.033}$    |
| h      | 0.06193488 | 0.00567 | $0.331^{+0.056}_{-0.049}$    | $0.773^{+0.026}_{-0.027}$    |

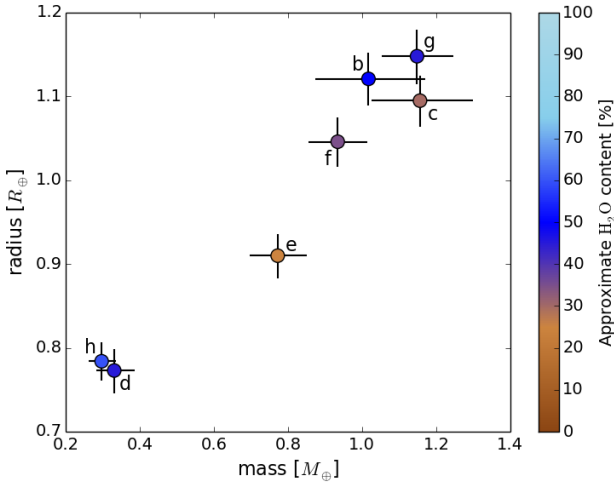


**Figure 1.** Mass-radius relationship of the TRAPPIST-1 planets from [Grimm et al. \(2018\)](#). Colours represent estimated  $\text{H}_2\text{O}$  content (including liquid water, ice and high-pressure polymorphs) in volume fraction (percentage), based on the calculations for representative cases in the work of [Dobos et al. \(2019\)](#).

ment of inertia around the planets’ principal rotation axis,  $M_{\text{pl}}$  is the planet’s mass, and  $R_{\text{pl}}$  is its radius ([Mignard 1979](#)). In the orbital stability studies of [Gillon et al. \(2017\)](#) and [Luger et al. \(2017\)](#), terrestrial and lunar values were used for the tidal parameters ([Lambeck 1980](#); [Néron de Surgy & Laskar 1997](#); [Bolmont et al. 2015](#)) for all of the TRAPPIST-1 planets. In reality the tidal quantities depend sensitively on the planets’ interior structures and thermal states (e.g., [Peale & Cassen 1978](#); [Lambeck 1980](#); [Segatz et al. 1988](#)), which have been shown to be substantially different from that of the Earth and Moon ([Barr et al. 2018](#)).

Here, we independently calculate two estimates for the tidal parameters of the innermost two TRAPPIST-1 planets using a combination of N-body dynamics and the simple four-component compositional model from [Dobos et al. \(2019\)](#). We provide estimates for the tidal quality factor  $Q$  and  $\frac{k_2}{Q}$  from both models that are consistent with the interior geodynamics, and discuss the agreement between the two approaches.

## 2 CURRENT DYNAMICAL STATUS OF THE TRAPPIST-1 SYSTEM

The TRAPPIST-1 system is one of the few known systems in which most of the planets are in an orbital mean-motion resonance with each other. It is characterised by at least four two-body mean-motion resonances as well as up to five three-body resonances ([Luger et al. 2017](#)). We test whether these resonances still can be seen in the latest observed physical and orbital parameters (see Table 1 and Figure 1) from [Grimm et al. \(2018\)](#). We simulate the system with nominal parameters for 100 years and 100 kyrs respectively with the SWIFT MVS software package ([Levison & Duncan 1994](#)). We do not investigate stability of the nominal system on longer timescales. The effect of general relativity is included for the periastron precession ([Nobili & Will 1986](#)). The time step is set to 0.03625 days. We set the mutual inclinations ( $i$ ) and longitudes of the ascending nodes ( $\Omega$ ) to 0 for all planets. We find that planets d to g are trapped in sequential two-body mean-motion resonances, and a resonance also involves planet h since their resonant angles ( $\phi$ ) librate. These resonances are

$$\begin{aligned}
 \phi_{\text{de}1} &= 3\lambda_e - 2\lambda_d - \varpi_d, \\
 \phi_{\text{de}2} &= 3\lambda_e - 2\lambda_d - \varpi_e, \\
 \phi_{\text{ef}1} &= 3\lambda_f - 2\lambda_e - \varpi_e, \\
 \phi_{\text{ef}2} &= 3\lambda_f - 2\lambda_e - \varpi_f, \\
 \phi_{\text{fg}1} &= 4\lambda_g - 3\lambda_f - \varpi_f, \\
 \phi_{\text{fg}2} &= 4\lambda_g - 3\lambda_f - \varpi_g, \\
 \phi_{\text{gh}1} &= 3\lambda_h - 2\lambda_g - \varpi_g,
 \end{aligned}$$

where  $\lambda = M + \varpi$  is the mean longitude, with  $M$  being the mean anomaly,  $\varpi = \omega + \Omega$  is the longitude of periastron and  $\omega$  is the argument of periastron. The last remaining resonance angle,  $\phi_{\text{gh}2} = 3\lambda_h - 2\lambda_g - \varpi_h$ , does not librate. Figure 2 shows the evolution of the resonant angles with time for 100 yr, indicating libration for all but one of the resonant angles. The libration period of the resonant angles is approximately 1.4 years.

The resonant angles can be manipulated to compute  $\Delta\varpi = \varpi_i - \varpi_j$  between any two planets. The results are displayed in Figure 3. Generally each consecutive pair of planets is approximately anti-aligned ( $\Delta\varpi \sim 180^\circ$ ) but other non-sequential pairs are librating around values approximately  $60^\circ$  away from 0. Alignment with planet d is sometimes broken into circulation because of secular forcing from planets b and c. Secular perturbations generally make the longitudes of periastron progress with time ( $\dot{\varpi} > 0$ ) but in a mean motion resonance generally the periastra regress ( $\dot{\varpi} < 0$ ) ([Murray & Dermott 1999b](#)). For the resonant planets the regression period is also equal to the libration period of the resonant angle i.e. 1.4 years, so that the regression is about  $\dot{\varpi} = -951\,000$  ''/yr, or approximately 4.61 rad/yr. This is between 0.8% to 3% of the orbital motion of planets d to g. Planets b and c are not tied to any of the resonances and their longitudes of periastron progress with a period of about 40 years. For planet h the precession is 350 years. These precession periods correspond to frequencies of 30 000 ''/yr and 3700 ''/yr respectively.

The planets are also caught in several three-body resonances ([Luger et al. 2017](#)). These are

$$\begin{aligned}
 \theta_{\text{bcd}} &= 2\lambda_b - 5\lambda_c + 3\lambda_d, \\
 \theta_{\text{cde}} &= \lambda_c - 3\lambda_d + 2\lambda_e, \\
 \theta_{\text{def}} &= 2\lambda_d - 5\lambda_e + 3\lambda_f, \\
 \theta_{\text{efg}} &= \lambda_e - 3\lambda_f + 2\lambda_g,
 \end{aligned}$$

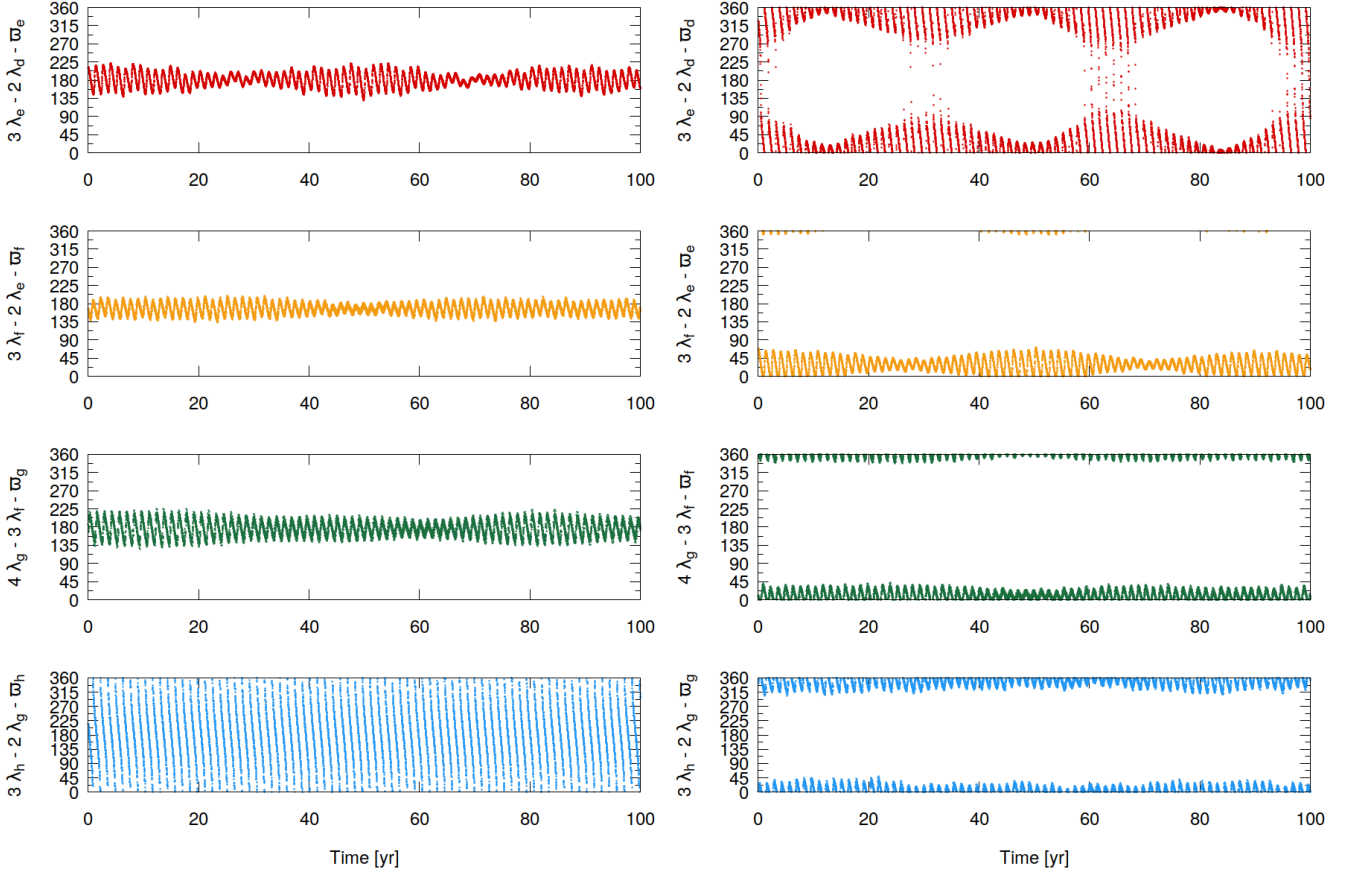


**Figure 2.** Evolution of the two-body resonant angles. With one exception in the bottom left panel showing the resonance angle  $\phi_{gh2}$ , all the rest librate with a period  $\sim 1.4$  years.

$$\theta_{fgh} = \lambda_f - 2\lambda_g + \lambda_h. \quad (1)$$

and are the result of combining the angles of two consecutive two-body resonances. The short-term variation of these angles is plotted in Figure 4. On longer timescales, however, all of the three-body resonances break (see Figure 5). We find that this typically happens after a few tens of thousands of years, much earlier than found by Grimm et al. (2018). We do not know what methodology and initial conditions they employed to keep the three-body angles librate for more than a million years. In contrast, the two-body resonant angles appear stable for at least 100 kyr.

When the system leaves the three-body resonances, the semi-major axes of the planets exhibit irregular jumps (Figure 6). Unlike the planets in the solar system, for which the semi-major axes are constant, the TRAPPIST-1 system is caught in multiple resonances which affect the semi-major axes. Since none of the major planets in the solar system are resonant, the system is governed by secular interaction rather than resonant interaction, and the former preserves the semi-major axes (Murray & Dermott 1999b). The irregular jumps in the semi-major axes of the TRAPPIST-1 planets are attributed to three-body resonance overlap (Quillen 2011), and the system is therefore chaotic. A very rough estimate of the longevity of the system against chaotic diffusion in semi-major axes is given by the time it takes for the semi-major axes to wander a distance approximately equal to the interplanetary spacing. Two estimates

of this timing are given by (Quillen 2011; Quillen & French 2014)

$$\begin{aligned} \tau_{11} &\sim 0.125\mu^{-3}\delta^6 |\ln \delta|^{-3}, \\ \tau_{12} &\sim \mu^{-3}\delta^{15/2}, \end{aligned} \quad (2)$$

where  $\mu = m_p/M_*$  and  $\delta = \alpha_{jk}^{-1} - 1$  is the interplanetary spacing, with  $\alpha_{jk} = \min(a_j/a_k, a_k/a_j)$  depending on the indices  $j$  and  $k$ . For TRAPPIST-1 typically  $\mu \sim 2 \times 10^{-5}$  and  $\delta \sim 0.3$  so that  $\tau_{11} = 6.7$  Gyr and  $\tau_{12} = 15$  Gyr. A stability time of 10 Gyr would require  $\delta > 0.27$  (Faber & Quillen 2007), which is satisfied for all pairs except f and g. Given that the age of the system is about 8 Gyr (Burgasser & Mamajek 2017), in the absence of tidal relaxation, the system could be close to instability, although the low angular momentum deficit (AMD) of the system would prevent a global instability (Laskar 1997).

### 3 THE POSSIBLE FORMATION OF THE TRAPPIST-1 SYSTEM

Ormel et al. (2017) have performed the most in-depth study of the formation of the TRAPPIST-1 system based on pebble accretion. They conclude that a mixture of said accretion and type 1 migration will place the planets in a multi-resonant configuration. The lack of resonances among the inner three planets is readily explained by the inner planets having been nudged outwards by the edge of the protoplanetary disc due to magnetic rebound (Liu et al. 2017).

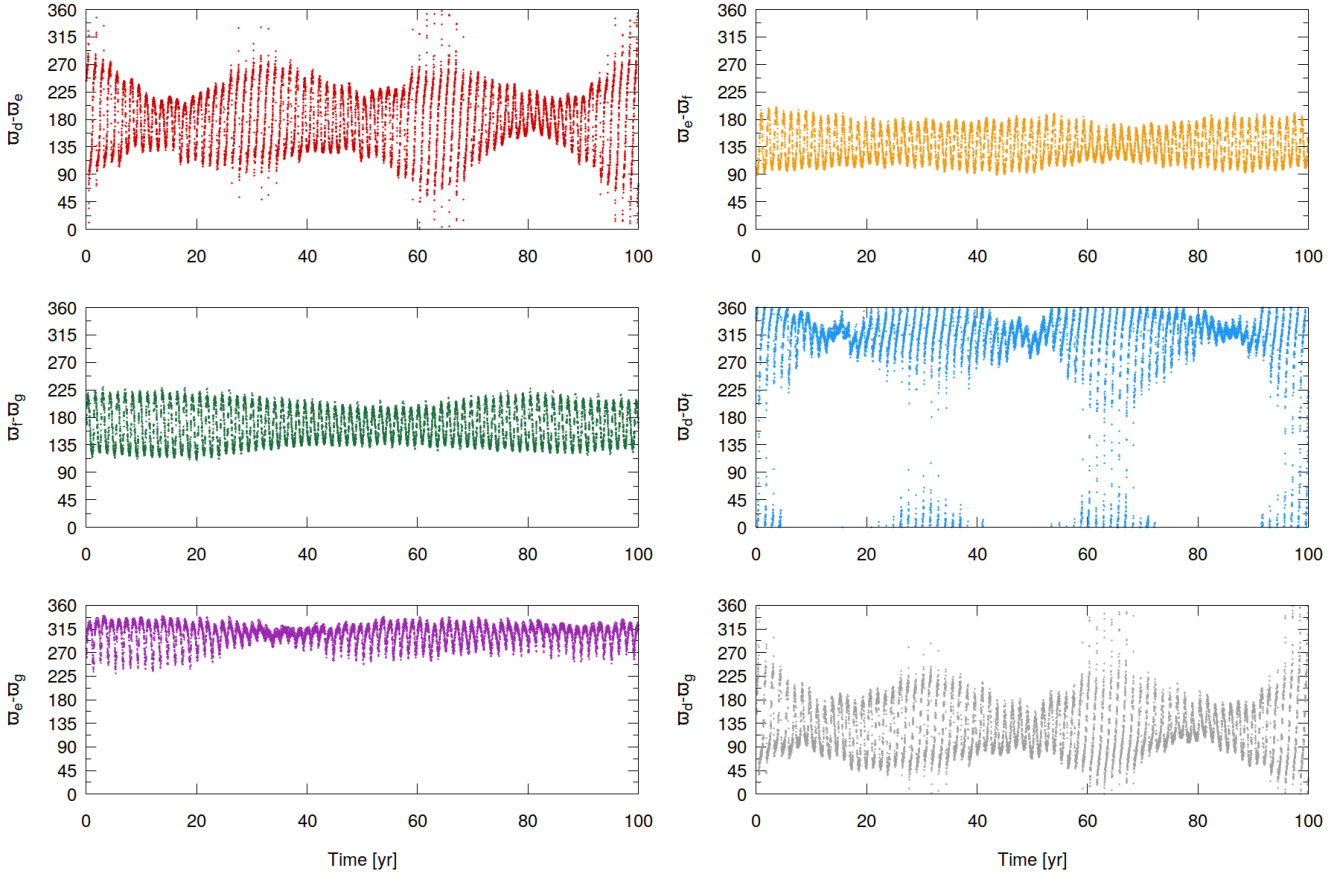


**Figure 3.** Apsidal anti-alignments for each planet pairs from planets d to g.

While this demonstrates several arguments in favour of forming the TRAPPIST-1 system with pebble accretion, the study by [Ormel et al. \(2017\)](#) just assumes that the planets migrate into resonances and forgoes performing a more in-depth study of the dynamics of this resonant trapping and its consequences. While a very detailed analysis of this effect is a study in itself, here we build a plausible argument for what the orbital structure of the TRAPPIST-1 system could have been before and shortly after the dispersal of the protoplanetary disc.

For simplicity we assume steady-state accretion of the disc gas onto the star. The gas accretion rate is related to the gas surface density and scale height of the disc via

$$\dot{M}_* = 3\pi\alpha_{\text{acc}}\Sigma H^2\Omega_K, \quad (3)$$

where  $\Sigma$  is the gas surface density,  $H$  is the disc scale height and  $\Omega_K$  is the Kepler frequency. The viscosity  $\nu = \alpha_{\text{acc}}c_s^2\Omega_K$  ([Shakura & Sunyaev 1973](#)), where  $\alpha_{\text{acc}}$  is an ‘effective’ parameter for global angular momentum transfer of the disc, which is assumed to be constant. The disc scale height is related to the temperature via  $H = c_s/\Omega_K$  where  $c_s^2 = (k_B T/\mu m_p)$  is the isothermal sound speed,  $k_B$  is the Boltzmann constant,  $m_p$  is the proton mass, and  $\mu = 2.3$  is the mean atomic mass of the gas.

For simplicity we make use of the disc model from [Ida et al. \(2016\)](#), which is based on the works of [Garaud & Lin \(2007\)](#) and [Oka et al. \(2011\)](#), but the analysis below can also be applied to more complex disc models. The disc is assumed to be in a steady state and the temperature and surface density are power laws of the

distance to the star. The best fit for the temperature profile is given by ([Garaud & Lin 2007](#); [Ida et al. 2016](#))

$$T = 150L_*^{2/7}M_*^{-1/7}\left(\frac{r}{1\text{ AU}}\right)^{-3/7}\text{ K}. \quad (4)$$

The unit of the stellar mass and stellar luminosity are the current solar values. The disc is assumed to be heated by the stellar flux, which generally applies to the outer portions of the disc. From the above temperature relation the reduced scale height becomes

$$h = 0.025L_*^{1/7}M_*^{-4/7}\left(\frac{r}{1\text{ AU}}\right)^{2/7}. \quad (5)$$

The surface density then follows from the steady state accretion and we have  $p = -d\ln\Sigma/d\ln r = 15/14$ . The nominal luminosity of pre-main sequence M-dwarf stars is  $L_* \sim M_*^2$  and thus in the first 1-10 Myr after the birth of TRAPPIST-1 the luminosity is  $L_* \sim 0.01 L_\odot$  ([Baraffe et al. 2015](#)). A value of  $\alpha_{\text{acc}} = 10^{-3}$  is consistent with the minimum-mass solar nebula (MMSN) when the stellar accretion rate is  $\dot{M} = 10^{-8} M_\odot \text{ yr}^{-1}$  ([Ida et al. 2016](#)), which corresponds to a stellar age of about 1 Myr ([Hartmann et al. 1998](#)). Furthermore, the stellar accretion rate  $\dot{M}_* \propto M_*^2$  ([Manara et al. 2015](#)). For the young TRAPPIST-1 we then have that at 1 Myr  $\dot{M} \sim 10^{-10} M_\odot \text{ yr}^{-1}$  and  $h \sim 0.023$  at 0.06 AU, and with these parameters our disc model is generally valid when  $r \gtrsim 0.06$  AU. For comparison, [Ormel et al. \(2017\)](#) adopted a constant reduced scale height of 0.03, which with our prescription occurs at about

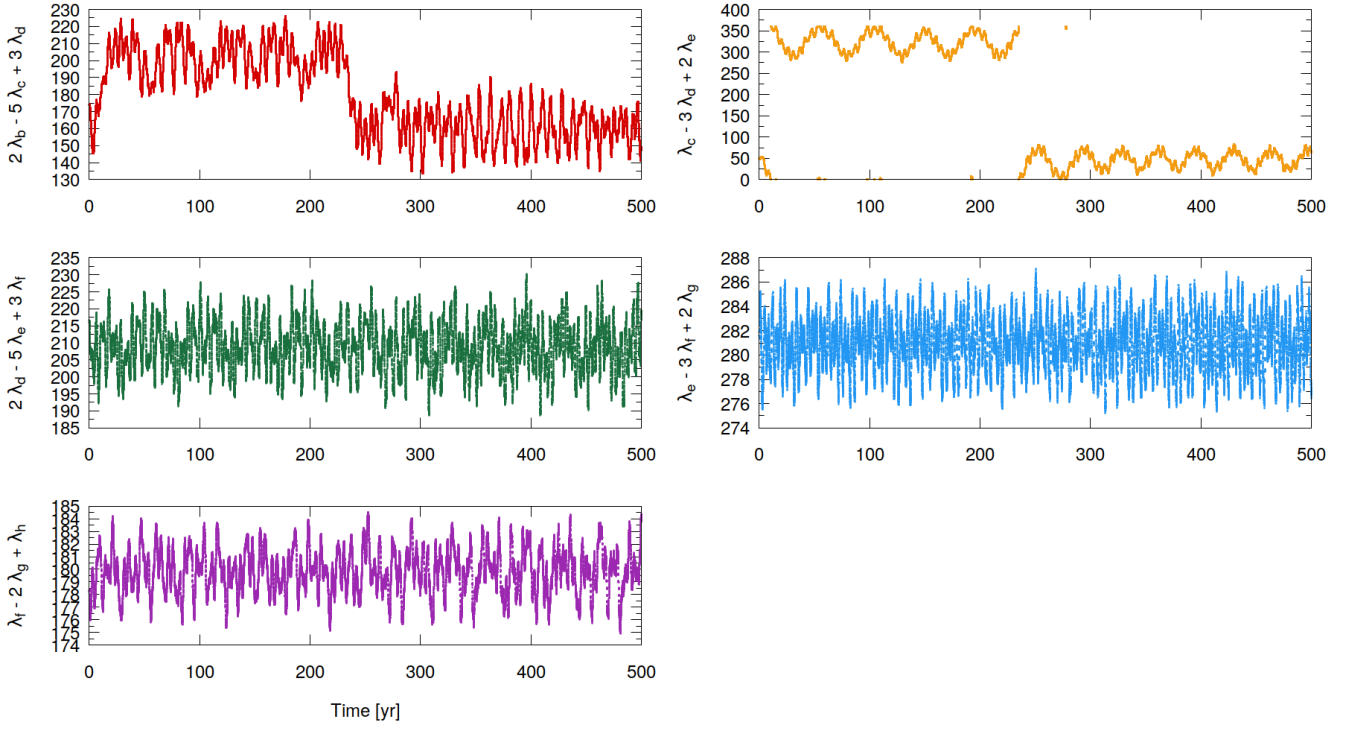


**Figure 4.** Three-body resonance angles on a short time-scale (500 years).

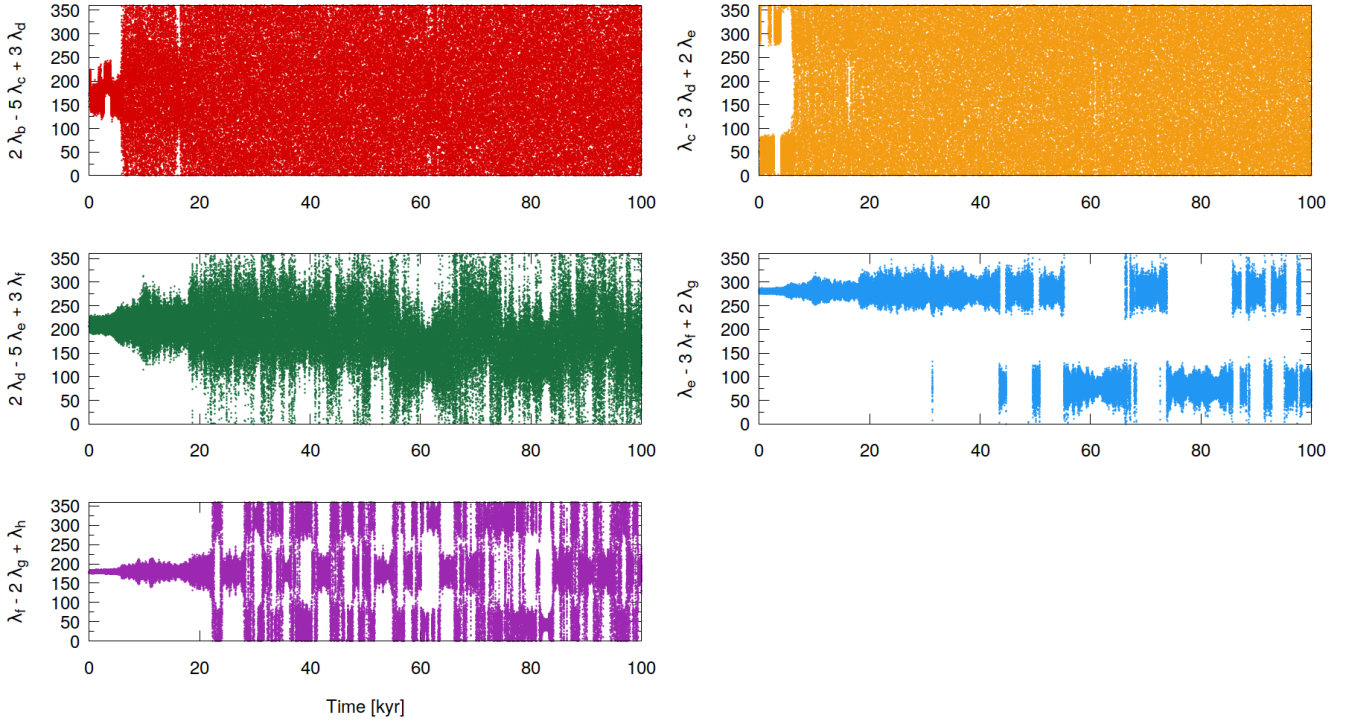


**Figure 5.** Three-body resonance angles on a long time-scale (100 000 years).

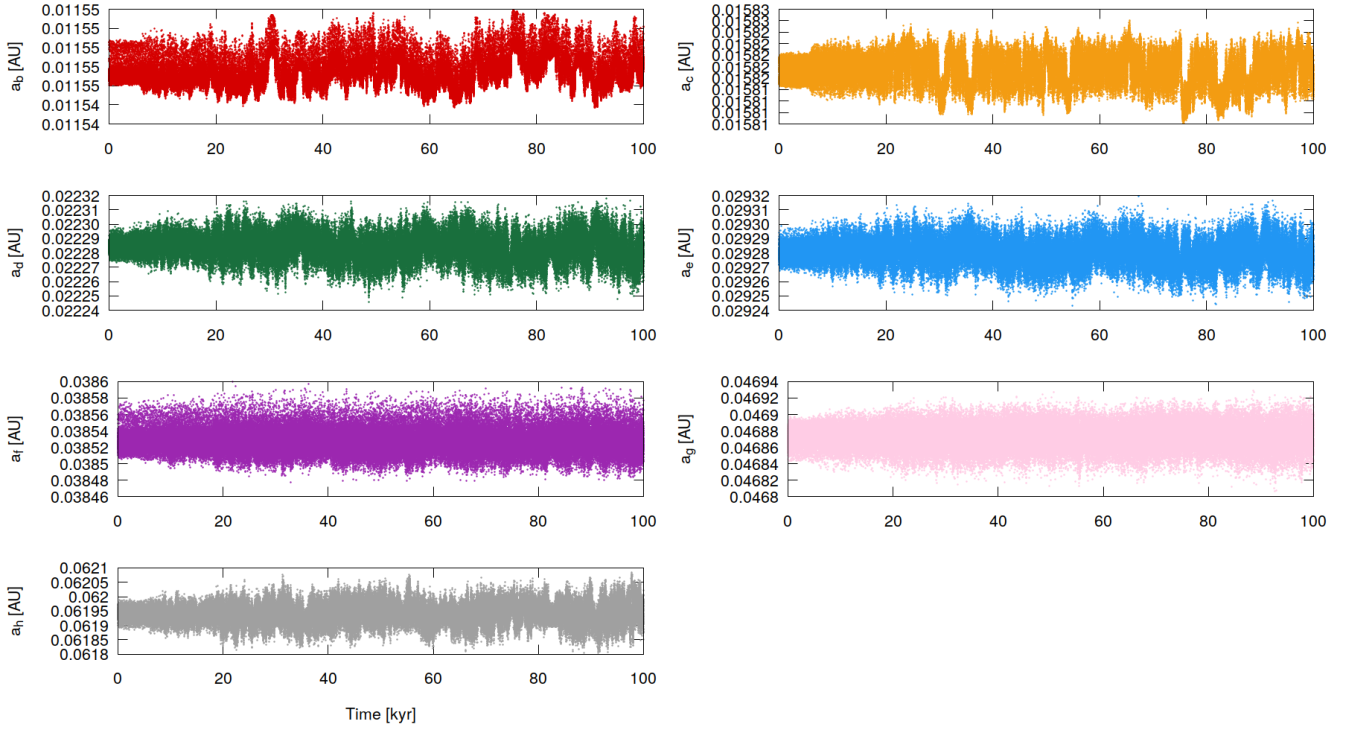


**Figure 6.** Semi-major axes of the planets' orbit on a long time-scale (100 000 years).

0.15 AU. [Unterborn et al. \(2018\)](#) adopted a nearly identical disc prescription to ours.

It is likely that the TRAPPIST-1 planetary system migrated inwards to its current location ([Unterborn et al. 2018](#)). If this system formed through pebble accretion ([Ormel et al. 2017](#)), then the migration was likely stalled by the innermost planet reaching the magnetic truncation of the disc ([Liu et al. 2017](#)) and the other planets all migrated into subsequent  $j + 1 : j$  mean-motion resonances. Resonance trapping occurs if the migration rate is slower than some critical value ([Petrovich et al. 2013](#)), i.e. when the rate of change of the mean motion  $\dot{n} \leq \dot{n}_{\text{crit}}$ , where  $n^2 = G(M_* + m_p)/r^3$  is the orbital frequency. This can be converted to a migration timescale  $\tau_c = n/\dot{n}$

$$\tau_c \geq \frac{26}{w_p} \frac{P}{10 \text{ d}} \left( \frac{M_{\oplus}}{m_p} \right)^{4/3} \left( \frac{M_*}{M_{\odot}} \right)^{4/3} \text{ kyr}, \quad (6)$$

where  $w_p$  is a numerical factor that depends on the resonance (1.33 for the 2:1 and 3.38 for the 3:2). If the planets are formed through pebble accretion ([Ormel et al. 2017](#)) then they are suggested to stop accreting solids when they reach the pebble isolation mass ([Lambrechts et al. 2014](#))  $m_{\text{iso}} = 0.5h^2 M_* \sim 1 M_{\oplus}$ . This is comparable to the thermal mass at which the planet opens a gap in the disc,  $m_{\text{gap}} = 6m_{\text{iso}} \sim 5M_{\oplus}$ . Planets above this mass will execute so-called type II migration ([Lin & Papaloizou 1986](#)), while lower-mass planets execute so-called type I migration ([Tanaka et al. 2002](#)). Since all planets are closer together than the 2:1 resonance, but usually not closer than the 3:2, this sets both an upper and a lower limit on the migration speed which is inconsistent with type II.

To lowest order in eccentricity, the type I migration timescale of the planets is given by

$$\tau_a^{-1} = 2\tau_m^{-1} + 2e^2\tau_e^{-1}, \quad (7)$$

where the eccentricity damping time scale is ([Cresswell & Nelson 2008](#))

$$\tau_e = 1.282t_{\text{wav}}(1 - 0.14\hat{e}^2 + 0.06\hat{e}^3), \quad (8)$$

where  $\hat{e} = e/h$ . We further have  $\tau_m = -L/\dot{L}$  which is given by

$$\tau_m = -\frac{t_{\text{wav}}}{\Gamma h^2} P_e, \quad (9)$$

where  $\Gamma = \dot{L}$  is the total torque (usually negative) and  $\tau_m < 0$  for outward migration. Here  $P_e$  is a function of eccentricity that takes care of supersonic corrections ([Cresswell & Nelson 2008](#))

$$P_e = \frac{1 + (0.444\hat{e})^{1/2} + (0.352\hat{e})^6}{1 - (0.495\hat{e})^4}. \quad (10)$$

The wave timescale is given by ([Tanaka & Ward 2004](#))

$$t_{\text{wav}} = \left( \frac{M_*}{m} \right) \left( \frac{M_*}{\Sigma r^2} \right) h^4 n^{-1}. \quad (11)$$

The total torque is the sum of the Lindblad and corotation torques. Accounting for the effect of saturation, in the subsonic case we have approximately  $\Gamma = 5.51q - 4.94$  ([Paardekooper et al. 2011](#)) where  $q = -\frac{d \ln T}{d \ln r}$ , whose nominal value is 3/7. At 0.1 AU for an  $1 M_{\oplus}$  planet  $t_{\text{wav}} \sim 40$  yr and the typical migration time is  $\tau_a \sim 12$  kyr. The critical migration time  $\tau_c = 1150$  yr, so the planets are expected to get trapped into resonances (since  $\tau_a > \tau_c$ ). In fact, it is expected that they should all be in the 2:1 resonance and the reason they passed over this resonance is because that configuration was probably overstable ([Goldreich & Schlichting 2014](#)). Once capture occurs, the inward migration of the planets is balanced by the resonances and any planet pair will be caught in a resonance wherein their equilibrium eccentricity is ([Goldreich & Schlichting 2014](#))

$$e_{\text{eq}}^2 = \frac{\tau_e}{(3j + 1.282)\tau_a}. \quad (12)$$

This leads to

$$\frac{\tau_e}{\tau_a} = 2.564|\Gamma|h^2. \quad (13)$$

With the nominal parameters,  $e_{\text{eq}} \approx 1.3h$ . Thus we expect the TRAPPIST-1 system to have migrated into a multi-resonant  $j+1 : j$  chain, with planets b and c possibly having been dislodged by a magnetic rebound (Ormel et al. 2017), where the eccentricities of all planets were comparable to the reduced scale height i.e. about 0.03.

#### 4 NUMERICAL SIMULATIONS OF LONG-TERM STABILITY

The current eccentricities are about a factor of 3-5 lower than what is predicted when the planets were initially captured in resonance. Thus we theorise that the current configuration could have only been reached after tidal damping of the initial eccentricities. However, the key to stability is the timescale of eccentricity damping. From numerical experiments lasting 100 Myrs, Izidoro et al. (2017) found that in excess of 75% of multi-resonant low-mass planetary systems go unstable in the absence of tidal damping; based on observational data from exoplanetary systems they further argue that as many as 95% multi-resonant systems must go unstable (cf. Goldreich & Schlichting 2014). This begs the question as to whether the primordial TRAPPIST-1 system, wherein the planets are all expected to have eccentricities  $e \approx h$ , was unstable as well, and if so, on what timescale. To test this hypothesis we perform simulations of the TRAPPIST-1 system for 100 Myrs wherein we systematically increase the initial angular momentum deficit (AMD) of the system. We choose this quantity rather than the individual eccentricities of the planets because the former is a measure of the dynamical excitation of the whole system rather than that of an individual planet. The normalised AMD is given by

$$\text{AMD} = \frac{\sum_k \mu_k \sqrt{a_k} (1 - \sqrt{1 - e_k^2})}{\sum_k \mu_k \sqrt{a_k}}. \quad (14)$$

Its value for the current orbital parameters is approximately  $2.6 \times 10^{-5}$ . We increase the initial AMD from 4 times to 21 times the current value, with the total AMD randomly partitioned amongst the planets; the upper value corresponds to all planets having an eccentricity of  $e \sim h$ . In these simulations we keep initial phases the same as those published in Grimm et al. (2018) to preserve the resonant structure. This allows us to investigate the effect of only the initial AMD on the instability timescale. The simulations are once again run with SWIFT MVS with the same parameters as in Section 2, but the total simulation time is increased to 100 Myrs. A system is defined to be unstable when we record an encounter between a pair of planets.

The outcome of these simulations are summarised in Figure 7, which shows the timescale to reach instability versus the initial AMD normalised by the current value. We find that half of all unstable cases have  $\text{AMD}/\text{AMD}_0 \lesssim 19$ , and that the median time for the system to go unstable is 27.5 Myrs. There is large scatter in the plot but there is also a clearly decreasing trend for the onset of instability with increasing AMD. Systems with  $\text{AMD}/\text{AMD}_0 \leq 13$  are generally stable for the duration of the simulation. Therefore, in absence of tidal dissipation, we expect the system to be unstable on a timescale of about 30 Myrs if all the planets originally had eccentricities comparable to the disc scale height. This sets an upper limit on the eccentricity damping timescale for the planets, and therefore on their interior structure and composition.

#### 5 TIDAL EVOLUTION AND ECCENTRICITY DAMPING TIMESCALES

To lowest order in eccentricity, the secular interaction between the planets follows the Laplace-Lagrange theory. This theory treats the planets as a set of coupled oscillators and can thus be reduced to an eigenproblem (Murray & Dermott 1999b). Here we follow the elegant approach of Batygin & Laughlin (2011) and Lovis et al. (2011) wherein tidal evolution and precession of the periape caused by tides and general relativity are considered too. Unfortunately, the Laplace-Lagrange theory does not work for resonant planets, because the resonant interaction increases the precession rate close to resonance and reverses its direction in resonance (Murray & Dermott 1999b). In Section 2 we showed that planets d to g are in multiple resonant chains, and that planets g and h are also in a resonance wherein one of the resonant angles librates. We deduced from our numerical simulations that the influence of the resonances causes the periapees of planets d to g to regress with periods of about 1.4 yrs. Secular coupling is the strongest between planets whose precession frequencies are close together and in the same direction (e.g. Murray & Dermott 1999b). As a result, secular coupling between the resonant quadruplet d to g is very strong and they form one secular group. However, these middle planets are only weakly coupled to planets b, c and h, which form the second secular group, because of the large disparity (and opposite direction) of the motion of the periapees of these two planet groups.

To emphasise the validity of this claim Figure 8 shows the Fourier decomposition of the eccentricity vectors of planets b, c, d and h. Since the motion appears to be chaotic, we chose to show the decomposition over 64 intervals of 4096 years each, for each planet, keeping only the 7 leading terms in the Fourier spectrum. Prominent frequencies are at 2000 "/yr, 4900 "/yr, 5800 "/yr, 6500 "/yr and 29500 "/yr. It is clear that for planet d the leading terms are associated with the resonance, but that other terms also play a role; the resonant term also shows up in the spectrum of planet h. For the innermost two planets, however, the resonant terms do not appear. As such, we resort to approximate the secular interaction for the whole system with the Laplace-Lagrange theory with the caveat that only the eigenfrequencies associated with planets b and c, and possibly h, are useful. The effect of the three-body resonances on the precession frequencies is similar to the two-body resonances (Quillen & French 2014).

Before we proceed a clarification is in order. In what follows we assume that the eccentricity evolution primarily occurs when the planets are in synchronous rotation. This is not entirely correct, because the tidal evolution on the planets will reduce both their eccentricities and their spin rates, and the planets may temporarily be trapped in spin-orbit resonances while their eccentricities are decreasing (Correia et al. 2014). However, the initial eccentricities after formation are expected to be of order 0.03, which are low enough that only temporary capture in the 3:2 spin-orbit resonance becomes feasible (Correia et al. 2014). An in-depth study of how the system evolves tidally with the planets locked in this spin-orbit configuration is beyond the scope of this paper.

Defining  $z = e \exp(i\varpi)$ , where  $i$  is the imaginary unit and  $\varpi = \Omega + \omega$  is the longitude of periape, without tides the equation of motion for the eccentricity and periape of planet  $j$  is

$$\dot{z}_j = \sum_{k=1}^N i A_{jk} z_k, \quad (15)$$

where the matrix  $\mathbf{A}$  contains the mutual interaction terms, which only depend on the masses and separation (Murray & Dermott

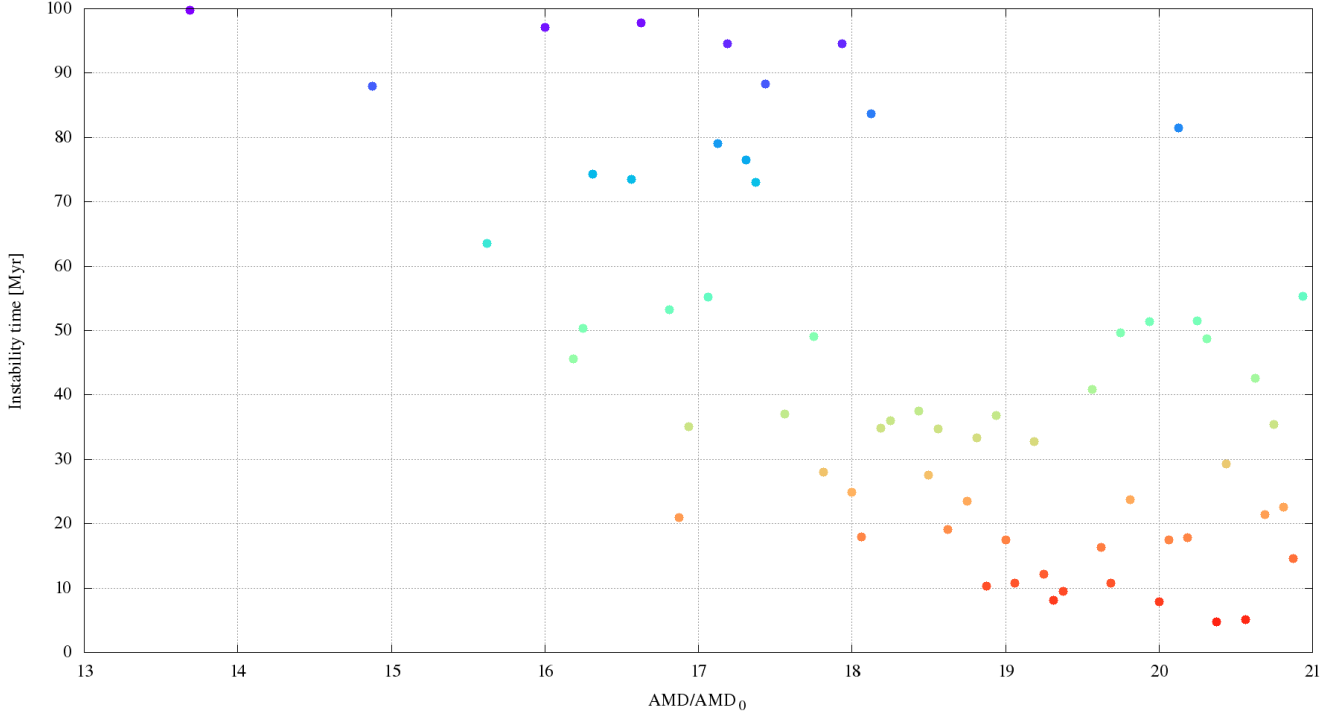


**Figure 7.** Instability time as a function of original AMD. The colours are there to aid visualisation.

1999b), and the effect of general relativity (Batygin & Laughlin 2011; Lovis et al. 2011). This system of equations has the solution

$$z_j = \sum_{k=1}^N \bar{e}_{jk} \exp[i(g_k t + \delta_k)], \quad (16)$$

where the  $g_k$  are the eccentricity eigenfrequencies and the  $\bar{e}_{jk}$  are the eigenvectors and  $\delta_k$  are initial phases.

To add in the tidal influence, we assume the eccentricities are damped according to  $\dot{z}_j = z_j/\tau_t^{(j)}$  (Batygin & Laughlin 2011), where  $\tau_t$  is the tidal damping timescale for each planet. It can be demonstrated from equation (159) in Boué & Efroimsky (2019) that for synchronous planets the frequency dependencies of the quadrupole quality functions  $k_{2j}/Q_j$  are model-independent. Consequently, for synchronous planets, the eccentricity damping timescales introduced by (Goldreich & Soter 1966) are also model-independent, and are given by

$$\tau_t^{(j)} = \frac{P_j}{21\pi} \frac{m_j}{M_*} \left(\frac{R_j}{a_j}\right)^{-5} \left(\frac{k_{2j}}{Q_j}\right)^{-1} \quad (17)$$

where  $P_j$  is the planet's orbital period,  $m_j$  is the mass,  $k_{2j}$  is the second degree Love number,  $Q_j$  is the tidal dissipation parameter,  $R_j$  is the radius and  $a_j$  is the semi-major axis of planet  $j$ . The effect of eccentricity damping by tidal friction within the planets can be modelled by adding an additional term to equation (15) as

$$\dot{z}_j = \sum_{k=1}^N (\iota A_{jk} + C_{jk}) z_k, \quad (18)$$

where  $C_{jj} = 1/\tau_t^{(j)}$  (Batygin & Laughlin 2011). The diagonal matrix  $\mathbf{C}$  adds a complex component to the eigenfrequencies. The solution is the same as equation (16), but eigenfrequencies  $g_k$  are now complex and the eigenvectors decrease with time. Furthermore, the

imaginary components of the eigenfrequencies are unequal, so that the decay timescale of several of the modes can be considerably longer than the shortest ones. Hence the system will eventually evolve to a state that has only a single secular eigenmode. The decay timescale of each eigenmode is (Batygin & Laughlin 2011)

$$\tau_d^{(j)} = [\text{Im}(g_j)]^{-1}. \quad (19)$$

The eigenmode decay timescale  $\tau_d^{(j)}$  can be far longer than the tidal damping timescale  $\tau_t^{(j)}$  so that even the innermost planets' orbits can stay eccentric for a long time because of secular coupling with the more distant planets (Batygin & Laughlin 2011; Lovis et al. 2011). Once the system only contains a single secular eigenmode, the rates of orbital precession are identical for all planets that are not in resonance. These orbits are either aligned or anti-aligned, depending on which particular eigenmode has survived. The orbital elements of the current system indicate that it has not yet reached that state. This is expected for planets d to g because they are in (three-body) resonances. The eccentricities of planets b, c and h are also inconsistent with zero, and of these only planet h is caught in a resonance.

The eigenfrequencies and associated eigenmodal damping times are listed in Table 2 as a multiple of the secular damping timescale in planet b ( $\tau_d^{(b)}$ ). Here we assumed that the lowest value of  $\tau_d^{(j)}$  corresponds to dissipation in planet b, the next shortest by dissipation in planet c, and so forth. Naturally some of the calculated frequencies make little sense because the resonant interaction is not taken into account, but for the frequencies corresponding to planets b, c and h this assumption is justified. The results in the table are based on an additional simplifying assumption that all the planets have the same composition and therefore the same rheology. This is demonstrably false (Unterborn et al. 2018; Barr et al.



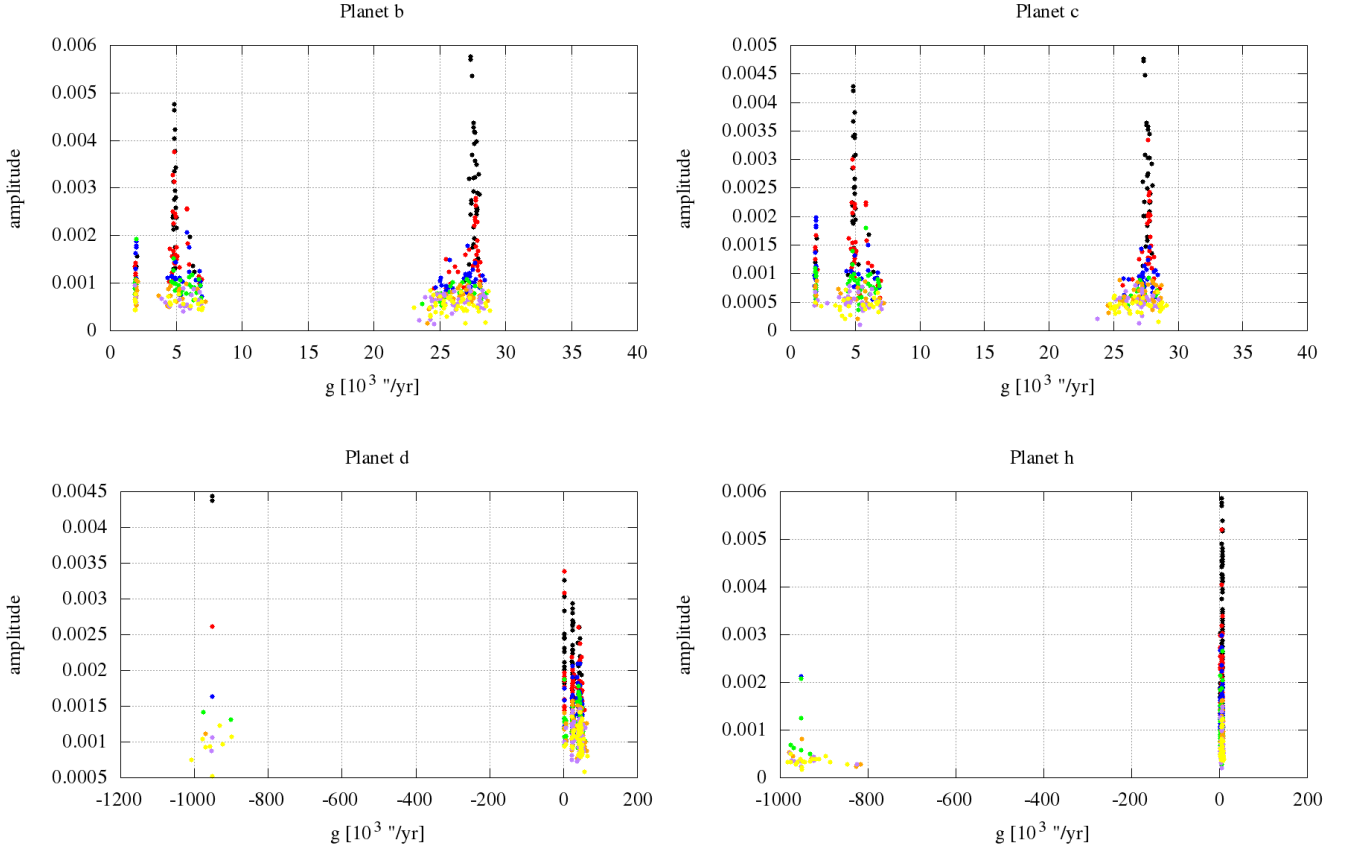


**Figure 8.** Fourier output of the eccentricity vectors of planets b, c, d and h for 64 intervals of 4096 years each. Only the 7 strongest modes were kept (depicted in black, red, blue, green, orange, indigo and cyan, respectively).

| planet | Eigenfrequency [ $^{\circ}$ /yr] | $\tau_d^{(j)}$ [ $\tau_d^{(b)}$ ] | $\tau_t^{(j)}$ [ $\tau_t^{(b)}$ ] |
|--------|----------------------------------|-----------------------------------|-----------------------------------|
| b      | 27300 ( $g_1$ )                  | 1.00                              | 1.00                              |
| c      | 4450 ( $g_2$ )                   | 1.58                              | 5.62                              |
| d      | 3370 ( $g_3$ )                   | 6.82                              | 82.7                              |
| e      | 8920                             | 9.73                              | 203                               |
| f      | 16500                            | 15.0                              | 521                               |
| g      | 15400                            | 25.2                              | 1060                              |
| h      | 1410 ( $g_7$ )                   | 30.9                              | 13700                             |

**Table 2.** Eigenfrequencies and eigenmode damping timescales. All of these frequencies are about 10%-30% lower than those computed with Fourier analysis from N-body simulations, primarily caused by near-resonances between planets b and c, planets c and d, and the circulation of  $\phi_{gh2} = 3\lambda_h - 2\lambda_g - \varpi_h$ .

2018; Dorn et al. 2018), but this simple example serves only as an indicator of the damping timescale disparity. Assuming that all the planets' interior temperatures are just above the solidus, their viscosities are  $\eta \sim 10^{14}$  Pa and rigidity  $\mu \sim 10$  GPa (Barr et al. 2018). Following Correia et al. (2014) we compute theoretical values of the tidal damping timescales  $\tau_t^{(j)}$  and modal damping timescales  $\tau_d^{(j)}$ . The actual values are, for now, unimportant; at present we are interested in their relative values only.

From this simple experiment it is clear that the mode that damps the slowest takes at least 30 times as long as the mode that

damps the fastest. This is in stark contrast to the ratio of the physical damping timescales in each of the planets, where the maximum ratio runs into the ten thousands. Significantly increasing or decreasing the damping efficiency in planets c to h while keeping the parameters for planet b fixed does not substantially change the values reported in the table, implying that most of the damping of the *whole system* occurs in planet b (and c). The disparate ratios of the values of  $\tau_t^{(j)}$  compared with  $\tau_d^{(j)}$  reinforce this claim. Unless damping in planet b is much less efficient than in planet c, the rate of eccentricity dissipation in planet c is expected to be about a third of that in planet b if they share a similar composition and tidal parameters.

We argue that if we want to keep the system dynamically stable within 100 Myrs to avoid breaking the resonance (Izidoro et al. 2017), and in light of the result given in Figure 7, the damping timescale in planet b cannot greatly exceed 10 Myrs, because we need to damp most of the AMD within 30 to 100 Myrs. This sets a lower boundary on the tidal parameters of this planet. Generally  $\tau_d^{(j)} \neq \tau_t^{(j)}$ , but for planet b they are comparable within a factor of two for a given composition because the term  $C_{11}$  dominates the secular motion of planet b in equation (18). Assuming these timescales are equal, assuming synchronous rotation and setting  $\tau_t^{(b)} \lesssim 10$  Myr implies that for planet b we have  $\frac{k_2}{Q} \gtrsim 2 \times 10^{-4}$ , which is lower than the measured values of Mars, the Moon and of the deep Earth. If we further assume that  $\tau_d^{(c)} = \tau_t^{(c)}$ , which is also correct within a factor of two for the rheologies assumed here, then

setting  $\tau_t^{(c)} \lesssim 10$  Myr for planet c we have  $\frac{k_2}{Q} \gtrsim 1 \times 10^{-3}$ , which is comparable to that in the Moon, Mars and deep Earth. In the next section we compare these values with those generated from interior models.

## 6 TIDAL PARAMETERS FROM INTERIOR MODELS

The response of a planet to tidal forcing is described by the three Love numbers,  $h_2$  and  $l_2$ , which describe tidal deformation, and  $k_2$ , which describes changes to the planet’s own gravitational potential due to the tidal deformation. For a viscoelastic body (Peltier 1974; Greff-Lefftz et al. 2005; Henning et al. 2009; Wahr et al. 2009; Efroimsky 2012; Barr et al. 2018),

$$k_2^* = \frac{3/2}{1 + \frac{19\mu^*}{2\bar{\rho}gR_{\text{pl}}}}, \quad (20)$$

where  $\bar{\rho}$  is the planet’s bulk density,  $g$  is its surface gravity, and the planet’s rigidity is  $\mu^* = M_1 + iM_2$ , where the star superscript denotes complex quantities. For simplicity we apply the Maxwell viscoelastic body model (Peltier 1974), for which

$$M_1 = \frac{\mu\nu^2\eta^2}{\mu^2 + \nu^2\eta^2}, \quad (21)$$

and

$$M_2 = \frac{\mu^2\nu\eta}{\mu^2 + \nu^2\eta^2}, \quad (22)$$

where  $\mu$  is the rigidity,  $\eta$  is viscosity, and  $\nu = 2n - 2\Omega_{\text{rot}}$  is the tidal forcing frequency, in this case,  $\nu = 2\pi/P$ , where  $P$  is the orbital period of each planet. The Maxwell model does not adequately reproduce the tidal dissipation in cold planets such as Mars (Bills et al. 2005), but the innermost few TRAPPIST-1 planets are expected to have hot interiors (Barr et al. 2018) so that the application of the Maxwell model may be warranted. The overall behaviour of the planet is analogous to a damped, driven oscillator, being driven at frequency  $\nu$ . Dissipation is maximized when the forcing time scale,  $T_{\text{f}} = 2\pi/\nu$  is equal to the Maxwell time, which is ratio between the viscosity and rigidity, i.e.  $\tau_M = \eta/\mu$ .

We mimic the effect of a multi-component, layered planet using a single, approximate uniform viscosity and rigidity (Barr et al. 2018; Dobos et al. 2019),

$$\eta(T) \approx \phi_{\text{iw}}\eta_{\text{iw}} + \phi_{\text{hpp}}\eta_{\text{hpp}} + \phi_{\text{r}}\eta_{\text{r}}. \quad (23)$$

where  $\eta$  represents the viscosity of the material. The indices refer to different material layers in the body: “iw” for ice I and/or liquid water, “hpp” for high-pressure polymorphs, “r” for rock, and “Fe” for iron. We use a similar relationship to construct a single value of the shear modulus ( $\mu$ ) that approximates the behaviour of the entire planet (Barr et al. 2018; Dobos et al. 2019),

$$\mu(T) \approx \phi_{\text{iw}}\mu_{\text{iw}} + \phi_{\text{hpp}}\mu_{\text{hpp}} + \phi_{\text{r}}\mu_{\text{r}}. \quad (24)$$

We neglect the viscosity and rigidity of the planets’ iron cores because tidal deformation of, and thus dissipation in, the cores will be negligible due to the restoring force imposed by the rock and ice mantle that lies atop the core in each body (Henning et al. 2009).

The  $\eta$  and  $\mu$  for each of the constituent materials depend strongly on temperature. Governing parameters and equations describing the material behavior may be found in Barr et al. (2018) and are too cumbersome to repeat here in full detail. For the rocky component of the TRAPPIST-1 planets, we assume a compressed bridgmanite composition (Unterborn et al. 2018), consistent with

the lower mantle of the Earth, with a density  $\rho_{\text{r}} = 5500$  kg/m<sup>3</sup> (Dziewonski & Anderson 1981). The viscosity and rigidity of rock change as a function of temperature, with both quantities decreasing sharply for temperatures above the solidus ( $T_{\text{s}} = 1600$  K). Another sharp decrease occurs when the volume fraction of solid rock is equal to the volume fraction of melt, at which point the crystal/melt mixture behaves more like a liquid than a solid (Renner et al. 2000). For temperatures below the solidus, we assume that the viscosity of rock is controlled by the deformation rate due to volume diffusion (Karato et al. 1995; Solomatov & Moresi 2000). For ice I, we assume  $\rho_{\text{iw}} = 1000$  kg/m<sup>3</sup> and that the viscous creep is accommodated by volume diffusion (Goldsby & Kohlstedt 2001). Above the melting point, values for the viscosity of liquid water are used, and the rigidity is set to zero. For the high pressure ice polymorphs, we assume  $\rho_{\text{hpp}} = 1300$  kg/m<sup>3</sup>, which accounts for the possible presence of ice phases II through VII (Hobbs 1974). We assume that the viscosity of the hpp ices follows an approximate Newtonian flow law applicable to ices VI and VII, which are volumetrically dominant in the TRAPPIST-1 bodies (Barr et al. 2018). For the shear modulus for hpp ices, we use an average value over the range for which experimental data exists (Shimizu et al. 1996). For the density of iron,  $\rho_{\text{Fe}} = 12,000$  kg/m<sup>3</sup>, consistent with the density of Earth’s inner core (Dziewonski & Anderson 1981; Unterborn et al. 2018).

We compute the total amount of energy produced by tidal dissipation in each planet assuming once again that the planets are in synchronous rotation, so that the multiple tidal forcing frequencies are all equal to the orbital frequency. For this configuration the tidal dissipation is (Segatz et al. 1988),

$$\dot{E}_{\text{tidal}} = -\frac{21}{2}\text{Im}(k_2^*)\frac{R_{\text{pl}}^5 n^5 e^2}{G}, \quad (25)$$

where  $\text{Im}(k_2^*)$  is the imaginary part of  $k_2^*$  and  $G$  is the gravitational constant and  $n$  is the orbital frequency (which is equal to the rotation frequency). Combining equations (20), (21), and (22) to find the real and imaginary parts of  $k_2^*$ , we get

$$\text{Re}(k_2^*) = \frac{3}{2}\frac{2\beta(2\beta + 19M_1)}{(2\beta + 19M_1)^2 + (19M_2)^2}, \quad (26)$$

$$\text{Im}(k_2^*) = -\frac{3}{2}\frac{2\beta(19M_2)}{(2\beta + 19M_1)^2 + (19M_2)^2}, \quad (27)$$

where  $\beta = \bar{\rho}gR_{\text{pl}}$ . The magnitude of  $k_2^*$  is

$$|k_2^*| = \frac{3\beta}{[(2\beta + 19M_1)^2 + (19M_2)^2]^{1/2}}. \quad (28)$$

The tidal quality factor is then computed as  $Q = \text{Im}(k_2^*)/|k_2^*|$  (Segatz et al. 1988). Following the method of Mignard (1979), it is common to use the quantity  $k_2\Delta t$  to calculate tidal torques (e.g. Bolmont et al. (2015)), where  $k_2$  is the amplitude of  $k_2^*$  and  $\Delta t$  is the time lag between the application of the tidal force and the planet’s response to the forcing (Murray & Dermott 1999a). The conversion from a  $Q$ -model to a time lag model is given by

$$k_2\Delta t = \frac{|k_2^*|}{\nu Q} = \frac{\text{Im}(k_2^*)}{\nu}. \quad (29)$$

In our simplified case  $\nu = n$  and the computed value of  $\Delta t$  is specifically tied to this forcing frequency. The relationship above should be used with extreme caution, because it is not applicable to cold, mostly solid planets because the forcing frequencies are generally very different from the natural frequencies inside the body (Makarov 2015). As such, we provide the relationship for reference

only. We use the nominal planetary orbital and physical parameters together with the best-fit interior composition to evaluate  $\dot{E}_{\text{tidal}}$ , the tidal Love number and quality factor below.

We take into account all the possible interior structures of the TRAPPIST-1 planets as presented in the work of [Dobos et al. \(2019\)](#). It varies from the lowest density case to the highest, according to the possible mass and radius pairs (taking into account their error bars) from Table 1. This covers even unlikely cases where one of the constituent materials are not present in the body (for example  $\phi_r = 0$ ).

The left panel of Figure 9 illustrates how the  $Q$  value of TRAPPIST-1 b varies as a function of the rock mantle temperature. Here, we have assumed the best-fit values for mass and radius:  $M_b = 1.017M_\oplus$ ,  $R_b = 1.121R_\oplus$ . We look at a single representative interior model with  $\phi_r = 0.5$ ,  $\phi_{iw} = 0.01$ ,  $\phi_{hpp} = 0.41$ , and  $\phi_{Fe} = 0.08$ , chosen because of its mixed ice/rock composition. The value of  $Q$  changes by many orders of magnitude as the temperature of the rock mantle increases from 1000 K to 1800 K, so the behaviour of the interior of the planet in response to tides is worth discussing in detail. For an even more in-depth discussion see [Barr et al. \(2018\)](#).

Tidal dissipation arises in a solid planet because the tidal forces drive the planet to deform, doing work against its own internal rigidity and self-gravity. For temperatures below the solidus,  $\eta$  and  $\mu$  are large, the planet is stiff and does not deform much in response to tidal forces. In this case,  $Q$  can be enormously high, with values of  $10^5$  or even  $10^6$ . At higher temperatures, the viscosity and rigidity of the bulk planet decrease, permitting more tidal deformation and dissipation. However, as the planet's temperature increases above the solidus ( $T_s = 1600$  K), the presence of melt in the planet's mantle causes the viscosity and rigidity to decrease. Tidal dissipation becomes less efficient. At temperatures well above the solidus, the viscosity and rigidity of the rock mantle are extremely low, so the internal rigidity of the planet is low, and tidal dissipation is small, leading once again to high  $Q$  values. Tidal dissipation is maximized when the mantle is at the solidus temperature, and  $Q \sim 300$ . However, the equilibrium mantle temperature, at which the tidal heat flux is equal to the convective heat flux, is larger than  $T_s$ ; in the case of TRAPPIST-1 b this temperature is  $T_{\text{eq}} = 1692$  K, which contains a melt fraction at which there is both strong tidal heating and efficient convective heat transport. For this structure and composition for planet b,  $Q = 5.65 \times 10^4$ ; we also compute  $|k_2^*| = 1.498$  and the Maxwell time  $\tau_M = 20.5$  d. The very high  $|k_2^*|$  value is caused by the presence of partial melt in the mantle.

To compare the behaviours of planets b and c, consider the  $Q$  value of TRAPPIST-1 c calculated for a reference case with  $M_{p1} = 1.156M_\oplus$ ,  $R_{p1} = 1.095R_\oplus$ ,  $\phi_{iw} = 0.009$ ,  $\phi_{hpp} = 0.328$ ,  $\phi_r = 0.5$ ,  $\phi_{Fe} = 0.163$ . In this case,  $T_{\text{eq}} = 1664$  K, cooler than planet b, and  $Q = 1.01 \times 10^4$ , a factor of 5 lower than the quality factor for planet b; for this planet  $|k_2^*| = 1.49$  and  $\tau_M = 26.9$  d.

The middle panel of Figure 9 illustrates how the  $Q$  values for TRAPPIST-1 b and c vary as a function of the rock volume fraction for all possible interior states. The width of the lines illustrate the uncertainty in  $Q$  due to uncertainties in the masses and radii of the planets, as well as the amounts of rock/metal/ice in their interiors. We find that TRAPPIST-1 b has  $Q = (4-20) \times 10^4$  for cases where  $\phi_r > 0.1$  (i.e., excluding the unlikely cases where the planet contains very little rock). TRAPPIST-1 c has  $Q = (0.7-3.7) \times 10^4$ . The values of  $k_2/Q$  range from  $(0.075-0.37) \times 10^{-4}$  for TRAPPIST-1 b and  $(0.4-2) \times 10^{-4}$  for TRAPPIST-1 c. This computed value of  $k_2/Q$  for planet b is lower than what was predicted from the dynamical simulations in the previous sections, but

the agreement between these two approaches is still reasonable. The level of disagreement between the two computed values of  $k_2/Q$  for planet c is similar. The corresponding time delays are then  $k_2\Delta t = 0.04$  sec to 0.75 sec for planet b and  $k_2\Delta t = 0.6$  sec to 7 sec for planet c.

## 7 MOMENTS OF INERTIA AND PRECESSION FREQUENCIES OF SPIN POLES

The interior models presented in the previous section can be used to compute the polar moment of inertia of the planets and compare their internal mass distribution with known values for solar system bodies. The combination of the moment of inertia and tidal parameters allows us to constrain the precession constants of the spin poles of these planets, which could have implications for climate cycles.

The moment of inertia for a spherical planet about its principal rotation axis is ([Turcotte & Schubert 2002](#)),

$$C = \frac{1}{M_{p1}R_{p1}^2} \int_0^{M_{p1}} r^2 dm. \quad (30)$$

For a uniform-density sphere,  $C = 2/5$ , and values less than  $2/5$  indicate the concentration of high-density materials toward the centre of the planet. Assuming the planets are fully differentiated, which seems likely given their high rock fractions ([Friedson & Stevenson 1983](#)) and tidal heat budgets ([Barr et al. 2018](#)), the moment of inertia integral can be evaluated for each distinct compositional layer, giving

$$C = \frac{2}{5} \left[ z_{Fe}x_r^5 + z_r(x_h^5 - x_r^5) + z_h(x_i^5 - x_h^5) + z_i(1 - x_i^5) \right], \quad (31)$$

where  $z_{Fe} = \rho_{Fe}/\bar{\rho}$ ,  $z_r = \rho_r/\bar{\rho}$ ,  $z_h = \rho_{hpp}/\bar{\rho}$ ,  $z_i = \rho_i/\bar{\rho}$ ,  $x_r = \phi_{Fe}^{1/3}$ ,  $x_h = (\phi_{Fe} + \phi_r)^{1/3}$ , and  $x_i = 1 - x_r - x_h$  (see the top right panel of Figure 10 for an illustration of the definition of the  $x$  values).

Figure 10 illustrates how the moment of inertia vary for each valid interior structure for planets b and c. We find that  $C$  ranges from  $\sim 0.235$  (extremely centrally condensed) to 0.4 (a homogeneous sphere). For comparison, in our Solar System, the solid planetary bodies have  $C \sim 0.31$  (Jupiter's moon Ganymede) to 0.38 (Jupiter's moon Callisto; [Schubert et al. 2004](#)); Earth has  $C = 0.33$  ([Turcotte & Schubert 2002](#)) and Mars has  $C = 0.366$  ([Bertka & Fei 1998](#)) while the Moon has  $C = 0.395$  ([Bolt 1960](#)). The gas giants have  $C \sim 0.25$  ([Helled et al. 2014](#)).

It should be noted that simply assuming a terrestrial value for the moment of inertia for all of the planets can cause the tidal torque to be overestimated by  $\sim 20$  to 50% ([Mignard 1979](#)). From our compositional models for the TRAPPIST-1 planets, it seems that  $C$  can be as low as 0.235, which can arise for planets whose interiors are composed of ice and iron and have very little rock. Taking into account geochemical arguments about the ratios of rock to metal ([Unterborn et al. 2018](#)) we may be able to rule out such extreme cases. For the representative cases (gray circles in Figure 10) we get  $C = 0.289$  for planet b and  $C = 0.286$  for planet c.

The moment of inertia values of planets b and c can be used to compute the precession frequencies of their spin poles. Tidal evolution should have placed the planets' obliquities in Cassini state 1, which has an obliquity near  $0^\circ$  ([Colombo 1966](#)), and their rotations into the synchronous state. Then, due to rotational and tidal deformation, the expected value of  $J_2$  is ([Correia & Rodríguez 2013](#))

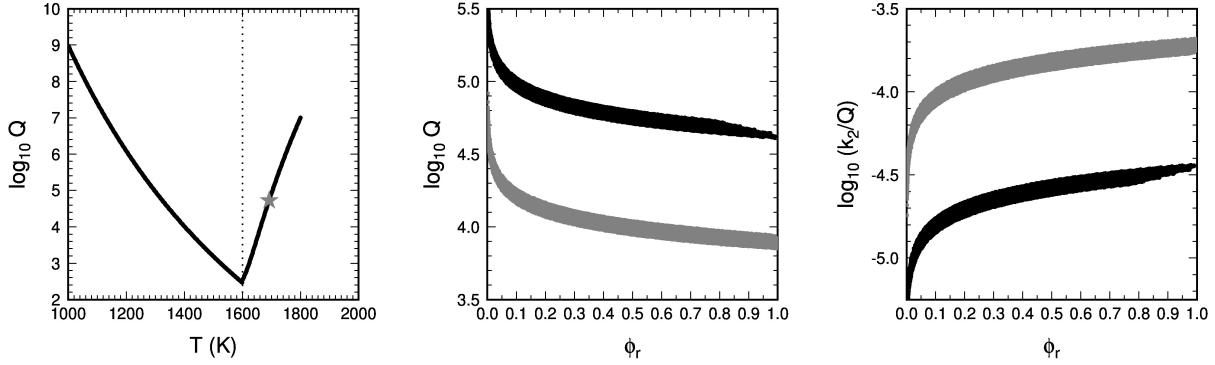


**Figure 9.** (left) Tidal quality factor ( $Q$ ) as a function of rock mantle temperature for a single representative model of TRAPPIST-1 b with  $M_{\text{pl}} = 1.017M_{\oplus}$ ,  $R_{\text{pl}} = 1.121R_{\oplus}$ ,  $\phi_r = 0.5$ ,  $\phi_{\text{hpp}} = 0.41$ ,  $\phi_{\text{iw}} = 0.01$ , and  $\phi_{\text{Fe}} = 0.08$ . The value of  $Q$  is minimized near the solidus temperature. The gray star indicates  $T = T_{\text{eq}}$  for this model planet. For temperatures lower than the solidus, the planet is too stiff to react to tidal flexing; conversely, for temperatures above the solidus, the presence of melt inhibits the dissipation of tidal energy as friction inside the planet. (middle) Values of  $Q$  (on a log scale) for a range of models of TRAPPIST-1 b (black) and TRAPPIST-1 c (grey) as a function of  $\phi_r$ . The  $Q$  value is evaluated for  $T = T_{\text{eq}}$  for each model planet. The width of the line represents uncertainties in  $Q$  due to uncertainties in the mass and radius of each planet, as well as the relative volume fractions of rock, metal, and ice. (right) Same as the middle panel, but depicting  $|k_2^*|/Q$  for each planet.

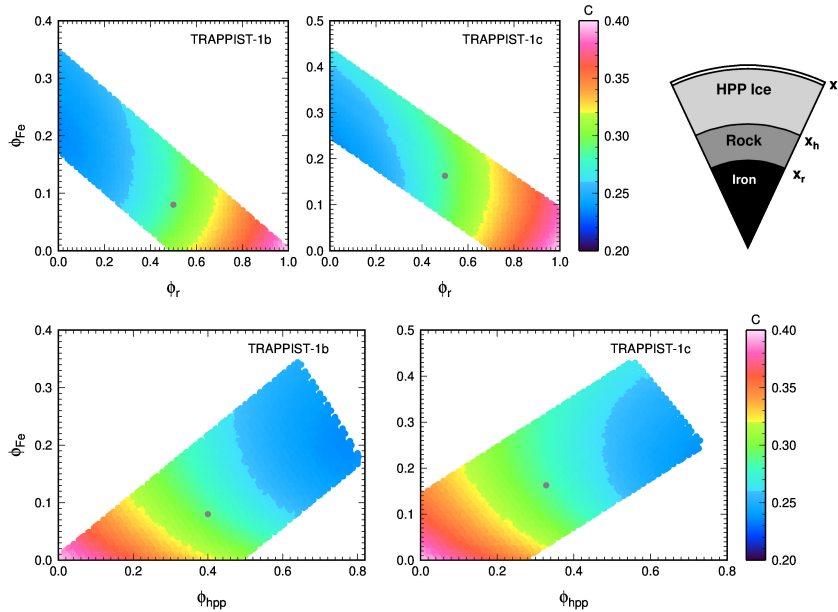


**Figure 10.** (top left) Colours show the values of the moment of inertia ( $C$ ) for each valid structure for TRAPPIST-1 b as a function of  $\phi_{\text{Fe}}$  and  $\phi_r$ . Values range from  $C \sim 0.25$  for rock- and iron-rich planets to  $C \sim 0.4$  for pure rock planets. Gray circle indicates the representative composition for TRAPPIST-1 b used to calculate  $Q$  in the left panel of Figure 9. (top middle) Same as top left panel, but for TRAPPIST-1 c. Gray circle indicates the representative compositional model for planet c. (top, right) Schematic illustration of the definitions of  $x_r$ ,  $x_h$ , and  $x_i$ . (bottom left) Values of  $C$  for TRAPPIST-1 b as a function of  $\phi_{\text{Fe}}$  and  $\phi_{\text{hpp}}$ . (bottom right) Same as bottom left panel, but for planet c.

$$J_2 = k_f \frac{n^2 R_{\text{pl}}^3}{GM_{\text{pl}}} + \frac{k_2}{2} \frac{M_*}{M_{\text{pl}}} \left( \frac{R_{\text{pl}}}{a} \right)^3, \quad (32)$$

where we have assumed  $e \approx 0$  and a zero obliquity. Our choice for the eccentricity is justified because for all the planets  $e < 0.01$  and the leading term in eccentricity for  $J_2$  is  $1 + \frac{3}{2}e^2$ . In the expression for  $J_2$ ,  $n$  is the mean motion, and  $k_f$  is the fluid Love number, which is related to the moment of inertia via the Darwin-Radau relationship,

$$C = \frac{2}{3} \left( 1 - \frac{2}{5} \sqrt{\frac{4 - k_f}{1 + k_f}} \right). \quad (33)$$

The precession frequency of the spin pole is given by (Colombo 1966)

$$\alpha = \frac{3}{2} n \frac{J_2}{C} (1 - e^2)^{-3/2}, \quad (34)$$

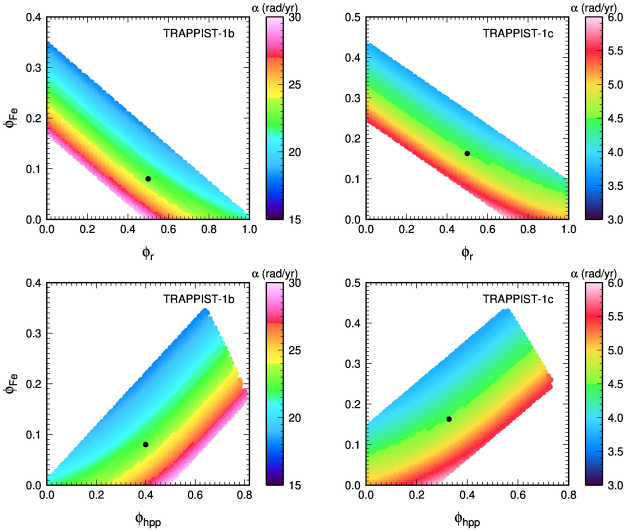


**Figure 11.** (top left) Colours show the values of the precession frequency for the spin pole for each valid structure for TRAPPIST-1b as a function of  $\phi_{Fe}$  and  $\phi_r$ . Black circle indicates the representative composition for TRAPPIST-1 b used to calculate  $Q$  in the left panel of Figure 9. (top right) Same as top left panel, but for TRAPPIST-1 c. (bottom left) Values of  $\alpha$  for TRAPPIST-1 b as a function of  $\phi_{Fe}$  and  $\phi_{hpp}$ . (bottom right) Same as bottom left panel, but for planet c.

where we assumed synchronous rotation.

Adopting the representative composition for TRAPPIST-1b, we obtain  $J_2 = 2.92 \times 10^{-3}$  and that  $\alpha = 23$  rad/yr, while for the representative case for planet c we have  $J_2 = 9.6 \times 10^{-4}$  and  $\alpha = 4.77$  rad/yr. The spin precession periods for both planets are shorter than an Earth year. These are faster than the eccentricity precession frequencies which exclude chaotic obliquity variations. For a full range of possible  $\alpha$  values obtained for the different possible interior structures, see Figure 11. For planet b,  $\alpha$  varies between 16 and 31 rad/yr, but for planet c the range is much smaller:  $3.5 < \alpha < 6.5$  rad/yr. The precession frequencies of the ascending nodes of these planets are expected to be similar in magnitude, but in the opposite direction, to their apsidal precession frequencies i.e. approximately  $-29000$  "/yr. As such, the spin precession frequencies of the poles are much faster than their nodes, and, apart from obliquities very close to  $90^\circ$ , we do not expect these planets to be in a secular spin-orbit resonance or to have a chaotic obliquity evolution.

## 8 DISCUSSION AND CONCLUSIONS

Although the TRAPPIST-1 planets experience tidal heat fluxes similar in magnitude to tidal heat fluxes experienced by Solar System objects like Io and Enceladus (Spencer et al. 2006; Howett et al. 2011; Barr et al. 2018; Dobos et al. 2019), the values of tidal quality factor,  $Q$ , are much larger than values estimated for Solar System objects. This is because the conversion of tidal energy to thermal energy is inefficient in a partially molten planetary mantle: the rigidity of the planet has decreased, so the planet experiences less internal friction. In the absence of prior estimates of  $Q$  for the TRAPPIST-1 planets,  $N$ -body simulations evaluating the stability of the orbits in the TRAPPIST-1 system have assumed Earth-like values:  $Q \sim$  a few hundred (Gillon et al. 2017; Bolmont

et al. 2015). This may lead to inaccurate estimates of the dynamical lifetime of the system (Gillon et al. 2017; Tamayo et al. 2017).

Here we have combined long-term  $N$ -body simulations with sophisticated tidal and thermal modelling. Specifically, for the  $N$ -body simulations we used initial conditions that are predicted from the formation of the TRAPPIST-1 system to study the system's dynamical stability. We found that the median instability time is close to 30 Myr, consistent with predictions of the dynamical lifetime of other such multi-resonant systems (Izidoro et al. 2017). Tidal secular theory predicts that the majority of the tidal dissipation of the system occurs in the innermost two planets. We used this theory and the dynamical instability timescale to constrain the tidal parameters of the inner two planets. We have found lower limits for the tidal parameter  $k_2/Q$ , having values above  $2 \times 10^{-4}$  for TRAPPIST-1 b and  $10^{-3}$  for TRAPPIST-1 c.

Additionally, we applied multi-layered viscoelastic deformation models of the type used to estimate tidal dissipation and stresses in the Earth and the Galilean and Saturnian satellites (Sabadini et al. 1982; Segatz et al. 1988; Roberts & Nimmo 2008; Wahr et al. 2009), to provide more realistic estimates of  $\text{Im}(k_2)$  and  $Q$  for the TRAPPIST-1 planets. We found that the fiducial interior model gives lower values for the  $k_2/Q$  tidal parameter of planets b and c (in the range of  $(0.08 - 0.37) \times 10^{-4}$  and  $(0.4 - 2) \times 10^{-4}$ , respectively) than obtained from the dynamical models.

The agreement is better if we increase the maximum eccentricity damping timescale from 30 Myrs to 100 Myrs because this would decrease the allowed minimum value of  $k_2/Q$  and for it to be more consistent with those calculated from the interior models.

In this work, however, we made several simplifying assumptions, first and foremost that all the planets are assumed to be synchronous throughout most of their evolution. As the planets spin down, they are expected to be temporarily trapped in spin-orbit resonances. From our numerical simulations the eccentricities of the TRAPPIST-1 planets remain at values near 0.01. As a result, planet c almost certainly spun down to the synchronous state, the probabilities of its capture in the 2:1 and 3:2 spin states being 0 and 0.02, correspondingly. At the same time, planet b could have been captured in the 2:1 spin-orbit resonance with a probability of as high as 0.2; its capture in the 3:2 spin-orbit resonance was certain had it skipped past the 2:1 (Makarov et al. 2018). It ensues from equation (156) in Boué & Efroimsky (2019) that, while in the synchronous and 3:2 spin-orbit resonances  $\dot{e} < 0$  always, in the 2:1 spin-orbit resonance this rate is positive (up to some caveats). Thus, had planet b been trapped in the 2:1 spin-orbit resonance, this planet's eccentricity was not decreasing but increasing during that capture. Should such eccentricity pumping have occurred it begs the question if this could have affected the stability of the whole system during the initial higher-eccentricity phase. Such an eccentricity increase would also increase the AMD of the system and this increase would need to be compensated by stronger damping in the other planets because the system did not undergo a global instability caused by excess AMD. We reserve an investigation of eccentricity damping versus pumping for future work.

The temporary trapping in the 3:2 spin-orbit resonance state has another consequence. In these higher spin-orbit resonance states the tidal dissipation rate is orders of magnitude higher than in the synchronous state, so that captured planets gradually heat up further, potentially alter their rheology, subsequently pop out of these spin-orbit resonant states and continue to despin towards the synchronous state. However, a heating of the interior appears to decrease the efficiency of tidal eccentricity damping, leading to a paradox as to how the system damped the excess eccentricity at

all. It is possible that most of the tidal damping happened in the 3:2 spin-orbit resonance configuration which could have changed the tidal parameters computed both from the dynamics and interior models, and when taking this into account the agreement between the two could be better.

Despite the somewhat different outcomes from the two models, we encourage the application of this two-method approach to constrain the tidal parameters of planets in other multi-resonant systems.

## ACKNOWLEDGEMENTS

The authors thank the reviewer Michael Efroimsky for useful questions and constructive comments that improved the quality of this manuscript. R. B. acknowledges financial assistance from the Japan Society for the Promotion of Science (JSPS) International Joint Research Fund (JP17KK0089) and JSPS Shingaku-jutsu Kobo (JP19H05071). V. D. is supported by the Hungarian National Research, Development, and Innovation Office (NKFIH) grants K-119993, K-115709, and GINOP-2.3.2-15-2016-00003. A. C. B. acknowledges support from NASA Habitable Worlds 80NSSC18K0136.

## REFERENCES

- Baraffe I., Homeier D., Allard F., Chabrier G., 2015, *A&A*, **577**, A42
- Barr A. C., Dobos V., Kiss L. L., 2018, *A&A*, **613**, A37
- Batygin K., Laughlin G., 2011, *ApJ*, **730**, 95
- Bertka C. M., Fei Y., 1998, *Earth and Planetary Science Letters*, **157**, 79
- Bills B. G., Neumann G. A., Smith D. E., Zuber M. T., 2005, *Journal of Geophysical Research (Planets)*, **110**, E07004
- Bolmont E., Raymond S. N., Leconte J., Hersant F., Correia A. C., 2015, *Astronomy & Astrophysics*, **583**, A116
- Bolt B. A., 1960, *Nature*, **188**, 1176
- Boué G., Efroimsky M., 2019, arXiv e-prints,
- Burgasser A. J., Mamajek E. E., 2017, *ApJ*, **845**, 110
- Colombo G., 1966, *AJ*, **71**, 891
- Correia A. C. M., Rodríguez A., 2013, *ApJ*, **767**, 128
- Correia A. C. M., Boué G., Laskar J., Rodríguez A., 2014, *A&A*, **571**, A50
- Cresswell P., Nelson R. P., 2008, *A&A*, **482**, 677
- Delrez L., et al., 2018, *Monthly Notices of the Royal Astronomical Society*
- Dobos V., Barr A. C., Kiss L. L., 2019, *A&A*, **624**, A2
- Dorn C., Mosegaard K., Grimm S. L., Alibert Y., 2018, *ApJ*, **865**, 20
- Dziewonski A. M., Anderson D. L., 1981, *Physics of the Earth and Planetary Interiors*, **25**, 297
- Efroimsky M., 2012, *ApJ*, **746**, 150
- Faber P., Quillen A. C., 2007, *MNRAS*, **382**, 1823
- Friedson A., Stevenson D., 1983, *Icarus*, **56**, 1
- Garaud P., Lin D. N. C., 2007, *ApJ*, **654**, 606
- Gillon M., et al., 2017, *Nature*, **542**, 456
- Goldreich P., Schlichting H. E., 2014, *AJ*, **147**, 32
- Goldreich P., Soter S., 1966, *Icarus*, **5**, 375
- Goldsby D., Kohlstedt D., 2001, *Journal of Geophysical Research: Solid Earth*, **106**, 11017
- Greff-Lefitz M., Métivier L., Legros H., 2005, *Celestial Mechanics and Dynamical Astronomy*, **93**, 113
- Grimm S. L., et al., 2018, *A&A*, in press,
- Hartmann L., Calvet N., Gullbring E., D'Alessio P., 1998, *ApJ*, **495**, 385
- Helled R., et al., 2014, *Protostars and Planets VI*, pp 643–665
- Henning W. G., O'Connell R. J., Sasselov D. D., 2009, *ApJ*, **707**, 1000
- Hobbs P. V., 1974, *Ice physics*. Oxford Clarendon Press
- Howett C. J. A., Spencer J. R., Pearl J., Segura M., 2011, *Journal of Geophysical Research (Planets)*, **116**, 3003
- Ida S., Guillot T., Morbidelli A., 2016, *A&A*, **591**, A72
- Izidoro A., Ogihara M., Raymond S. N., Morbidelli A., Pierens A., Bitsch B., Cossou C., Hersant F., 2017, *MNRAS*, **470**, 1750
- Karato S.-I., Zhang S., Wenk H.-R., 1995, *Science*, **270**, 458
- Khurana K. K., Jia X., Kivelson M. G., Nimmo F., Schubert G., Russell C. T., 2011, *Science*, **332**, 1186
- Lambeck K., 1980, Cambridge University Press, London, New York
- Lambrechts M., Johansen A., Morbidelli A., 2014, *A&A*, **572**, A35
- Laskar J., 1997, *A&A*, **317**, L75
- Levison H. F., Duncan M. J., 1994, *Icarus*, **108**, 18
- Lin D. N. C., Papaloizou J., 1986, *ApJ*, **309**, 846
- Liu B., Ormel C. W., Lin D. N. C., 2017, *A&A*, **601**, A15
- Lovis C., et al., 2011, *A&A*, **528**, A112
- Luger R., et al., 2017, *Nature Astronomy*, **1**, 0129
- Makarov V. V., 2015, *ApJ*, **810**, 12
- Makarov V. V., Berghea C. T., Efroimsky M., 2018, *ApJ*
- Manara C. F., Testi L., Natta A., Alcalá J. M., 2015, *A&A*, **579**, A66
- Mignard F., 1979, *The Moon and the Planets*, **20**, 301
- Murray C. D., Dermott S. F., 1999a, *Solar System Dynamics*. Cambridge University Press
- Murray C. D., Dermott S. F., 1999b, *Solar system dynamics*. Cambridge University Press
- Néron de Surgy O., Laskar J., 1997, *Astronomy and Astrophysics*, **318**, 975
- Nobili A. M., Will C. M., 1986, *Nature*, **320**, 39
- Oka A., Nakamoto T., Ida S., 2011, *ApJ*, **738**, 141
- Ormel C. W., Liu B., Schoonenberg D., 2017, *A&A*, **604**, A1
- Paardekooper S.-J., Baruteau C., Kley W., 2011, *MNRAS*, **410**, 293
- Peale S. J., Cassen P., 1978, *Icarus*, **36**, 245
- Peltier W., 1974, *Reviews of Geophysics*, **12**, 649
- Petrovich C., Malhotra R., Tremaine S., 2013, *ApJ*, **770**, 24
- Quillen A. C., 2011, *MNRAS*, **418**, 1043
- Quillen A. C., French R. S., 2014, *MNRAS*, **445**, 3959
- Renner J., Evans B., Hirth G., 2000, *Earth and Planetary Science Letters*, **181**, 585
- Roberts J. H., Nimmo F., 2008, *Icarus*, **194**, 675
- Sabadini R., Boschi E., Yuen D. A., 1982, *J. Geophys. Res.*, **87**, 2885
- Schubert G., Anderson J. D., Spohn T., McKinnon W. B., 2004, *Interior composition, structure and dynamics of the Galilean satellites*. Cambridge University Press, pp 281–306
- Segatz M., Spohn T., Ross M. N., Schubert G., 1988, *Icarus*, **75**, 187
- Shakura N. I., Sunyaev R. A., 1973, *A&A*, **24**, 337
- Shimizu H., Nabetani T., Nishiba T., Sasaki S., 1996, *Physical Review B*, **53**, 6107
- Solomatov V., Moresi L.-N., 2000, *Journal of Geophysical Research: Solid Earth*, **105**, 21795
- Spencer J. R., et al., 2006, *Science*, **311**, 1401
- Tamayo D., Rein H., Petrovich C., Murray N., 2017, *The Astrophysical Journal Letters*, **840**, L19
- Tanaka H., Ward W. R., 2004, *ApJ*, **602**, 388
- Tanaka H., Takeuchi T., Ward W. R., 2002, *ApJ*, **565**, 1257
- Turcotte D., Schubert G., 2002, *Geodynamics*, 456 pp. Cambridge Univ. Press, New York
- Unterborn C. T., Desch S. J., Hinkel N. R., Lorenzo A., 2018, *Nature Astronomy*, **2**, 297
- Wahr J., Selvans Z. A., Mullen M. E., Barr A. C., Collins G. C., Selvans M. M., Pappalardo R. T., 2009, *Icarus*, **200**, 188
- Wang S., Wu D.-H., Barclay T., Laughlin G. P., 2017, preprint ([arXiv:1704.04290](https://arxiv.org/abs/1704.04290))